*Journal of Advanced Ceramics*
2019, **8**(2): 238–246
https://doi.org/10.1007/s40145-018-0309-x
ISSN 2226-4108
CN 10-1154/TQ

**Research Article**

# $TiO_2/WO_3$ heterogeneous structures prepared by electrospinning and sintering steps: Characterization and analysis of the impedance variation to humidity

Evando S. ARAÚJO*, Victor N. S. LEÃO

*Research Group on Electrospinning and Nanotechnology Applications* (*GPEA-Nano*), *Department of Materials Science*, *Universidade Federal do Vale do São Francisco*, *48902-300*, *Juazeiro-BA*, *Brazil*

Received: July 6, 2018; Revised: November 25, 2018; Accepted: December 5, 2018
© The Author(s) 2019.

**Abstract:** Relative humidity (RH) is a critical environmental variable for transportation and storage of products and for the quality guarantee of several other production processes and services. Heterogeneous structures prepared from the selective semiconductor oxides may improve the sensitivity to humidity due to the better electronic and surface properties, when compared to pristine oxides. This work shows an alternative fabrication route for producing titanium dioxide/tungsten trioxide ($TiO_2/WO_3$) heterogeneous structures (by electrospinning and sintering) for potential application on the RH detection. The microstructural properties of the materials were analyzed by scanning electron microscopy (SEM), energy dispersive X-ray analysis (EDS), X-ray diffraction, and Raman spectroscopy. The electrical characterization of the structures was performed by electrical impedance spectroscopy in RH range of 10%–100%. Results indicated a p- to n-type conduction transition at around 30%–40% RH for all tested settings. The analysis of the impedance signature to humidity showed that the amount of fiber layers on the electrode and working temperature are important parameters to improve the humidity sensing of the $TiO_2/WO_3$ systems.

**Keywords:** electrospinning; heterogeneous structures; preparation; relative humidity; semiconductors

## 1 Introduction

In the last years, increasing interest has been devoted to the study of metal oxide semiconductors for use as sensors, photocatalysts, and energy conversion devices due to the electronic properties, excellent chemical stability, and high surface area to volume ratio [1,2].

The chemisorbed and physisorbed layers of water molecules on the semiconductor surface and the capillary condensation of water in the microscopic pores between particles can promote humidity-dependent electrical variations (due to electronic/ionic charge transfer reactions), which allows the application of these systems in relative humidity (RH) detection [3]. Recently, Zhang *et al.* [4–8] have shown important advances in the development of high-sensitivity humidity sensors, such as their hybrid nanostructures based on selective polymers, metal oxides, and graphene oxide.

Anatase titanium dioxide ( $TiO_2$ ) (~3.2 eV bandgap) is one of the most used metal oxides in RH sensors. This oxide is non-toxic with a high chemical stability and an excellent combination of photoactivity and

* Corresponding author.
E-mail: evando.araujo@univasf.edu.br

photostability. Heterogeneous metal oxide structures (produced by the sintering of mixtures of these oxides) are also shown as potential materials for the production of these sensors, considering the better physical and chemical properties of these heterogeneous materials when compared to those presented by the pure oxides. Selective semiconductors including zinc oxide ( ZnO ), vanadium pentoxide ( $V_2O_5$ ), niobium pentoxide ( $Nb_2O_5$ ), and tungsten trioxide ( $WO_3$ ) have been incorporated to $TiO_2$ to improve structural properties and sensitivity to RH [1,3,9,10].

The $TiO_2$ / $WO_3$ structures (in the form of volumetric pellets and sintered at 500 ℃, using gold electrodes as electric contact) have been used for RH detection [9,10]. The results indicated that the 1/1 in mole configuration preserves the phases of components and improves the electrical conduction process of the system over pure $TiO_2$ and $WO_3$ particles, which favors the humidity sensing.

An alternative to promote the adequate distribution of particles and increase the interaction of these oxides with the action medium has been to incorporate them into polymeric micro/nanofibers by the electrospinning technique [11], depositing layers of the composite on electrodes, with subsequent sintering of the resulting material (elimination of the organic phase) [12].

This alternative preparation route allows producing films of the resulting material arranged on electrodes instead of the usual volumetric disks or pellets, using a much smaller amount of semiconductor material than that used to produce volumetric species, without loss of sensorial quality.

In this work, we have used this alternative route for the preparation of $TiO_2$ / $WO_3$ heterogeneous structures as potential moisture sensing materials. The microstructure of the new systems was also investigated and associated to the obtained effects. A chemometric study was also performed to evaluate the importance of number of fiber layers and working temperature on the electrical variation to humidity, in the studied systems. The results show that this fabrication method is an important factor for increasing the humidity sensing efficiency of the system.

## 2 Materials and methods

### 2. 1 Materials

The materials poly (methacrylic acid-co-methyl methacrylate) (Evonik Industries), anatase titanium dioxide ( $TiO_2$ , < 150 nm particle size, Sigma Aldrich (Merk)), monoclinic tungsten trioxide ($WO_3$, < 100 nm particle size, Sigma Aldrich), and ethyl alcohol (99%) were used as received.

### 2. 2 Sample preparation

The oxides used in the detection of moisture were prepared by electrospinning and sintering steps. A schematic representation of the fabrication procedure is shown in Fig. 1.

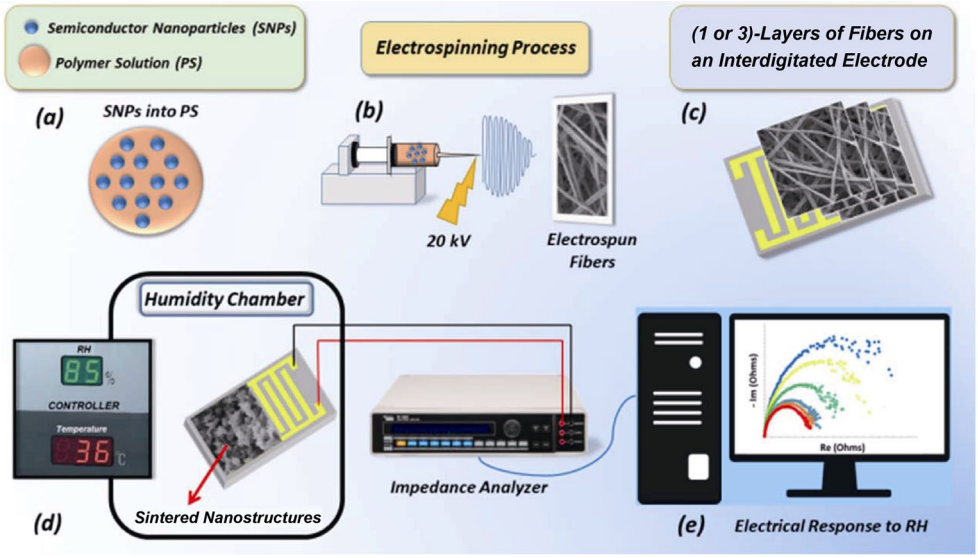


**Fig. 1** Scheme of the structure preparation and electrical characterization: (a) semiconductors into polymeric solution for the electrospinning process, shown in (b); (c) fiber layers arranged on a gold interdigitated electrode; (d) sintered $TiO_2$/$WO_3$ structures in a humidity chamber; (e) analysis of the electrical response to humidity.

For the electrospinning process, 0.25 g of $TiO_2/WO_3$ (1/1 in mole) are mechanically homodispersed in 2 mL of polymeric solution (produced from 1.4 g of the polymer in 6 mL of ethyl alcohol) using a mini rotating homogenizer. Then, the sample is transferred to a conventional syringe (capacity of 10 mL and metallic capillary needle diameter of 0.7 mm) under constant pressure (100 μL/min). An electric potential of the order of 20 kV is established between the tip of the needle and a grounded flat metallic collector (10 cm × 10 cm), separated by a typical distance of 10 cm. This configuration promotes the ejection of composite fibers from the tip of the needle to the collector (with respective solvent evaporation).

The metal oxide-containing fibers are produced in a 5 min interval, arranged in layers (1 and 3 layers) and deposited on a gold interdigitated electrode (1.1 cm × 1.0 cm) with the electric circuit arranged under an insulating substrate of alumina. Then, each sample deposited on the circuit is sintered in a muffle oven at 500 ℃ for 1 h to remove the organic matrix and obtain the final material (sintered $TiO_2$ / $WO_3$ structures). The interdigitated circuits containing the sintered materials are connected by electrical wires to the impedance analyzer to investigate the electrical response of the systems to relative humidity exposure in a humidity chamber (6.5 L capacity, RH and temperature automatic control, with a ±1% error) (Fig. 1).

### 2. 3 Microstructural and electrical signature

The microstructure of the produced materials was analyzed by scanning electron microscopy (SEM; Vega 3XM Tescan with dispersive energy detector X-ray (EDS) and Philips XL 30 TMP microscopes), X-ray diffractograms (XRD; Philips PW3040/00, Cu Kα, 1.54056 Å radiation) in the $2\theta$ range of 15° to 70°, and Raman spectroscopy (HORIBA Jobin Yvon, 532 nm laser, 20–25 mW). The identification of the crystalline phases was performed using the X-Pert HighScore software and the crystallographic data were obtained from the International Centre for Diffraction Data (ICDD).

The electrical characterization of the structures was investigated by electrical impedance spectroscopy, in the frequency range of 400 Hz to 40 MHz (impedance analyzer HP4194A, Hewlett-Packard). The samples were tested at the working temperatures of 20 and 30 ℃, with relative humidity values ranging from 10% to 100 % (per decade).

### 2. 4 Statistical analysis

Statistical analyses of fiber diameter and grain size of the sintered structures were performed on the images obtained by SEM, in ImageJ software.

The study of the relative importance of parameters on the electrical signature to humidity was performed in terms of a $2^2$ factorial design [13,14], by varying number of fiber layers ($L$, 1 and 3 layers) arranged on the electrode and working temperature ($T$, 20 and 30 ℃) of the systems.

The electrical response of the systems was evaluated in terms of the percentage variation of the impedance module ($|Z|$), $(Z_i–Z_f)/Z_i$. $Z_i$ represents the maximum value obtained from $|Z|$ in RH range and $Z_f$ is the value of $|Z|$ at 100% RH.

Each tested combination of the parameters was identified by the association of the symbols of the factors ($L$ and $T$). The presence of each one corresponds to the systems in which the parameters assume the maximum value (for example, $LT$ represents the sintered $TiO_2$ / $WO_3$ produced from 3 layers and tested at 30 ℃). Sample $I$ represents the system with the minimum values of the parameters. The relative importance of the number of layers ($L$) (Eq. (1)) characterizes the difference of average of $|Z|$ variation in the systems in which the maximum (3 layers) and minimum (1 layer) of $L$ factor are considered (see Table 2):

$$\text{Relative importance of } L = \frac{1}{2}(L + LT) - \frac{1}{2}(I + T) \quad (1)$$

Similarly, the importance of increasing the working temperature ($T$, 20–30 ℃) to the system response is given by Eq. (2):

$$\text{Relative importance of } T = \frac{1}{2}(T + LT) - \frac{1}{2}(I + L) \quad (2)$$

## 3 Results and discussion

### 3. 1 Microstructural characterization

SEM images and EDS mapping of $TiO_2/WO_3$ structures produced by electrospinning and sintering are shown in Fig. 2. Statistical analyses were performed on the three samples of each tested configuration, using a 95% confidence level.

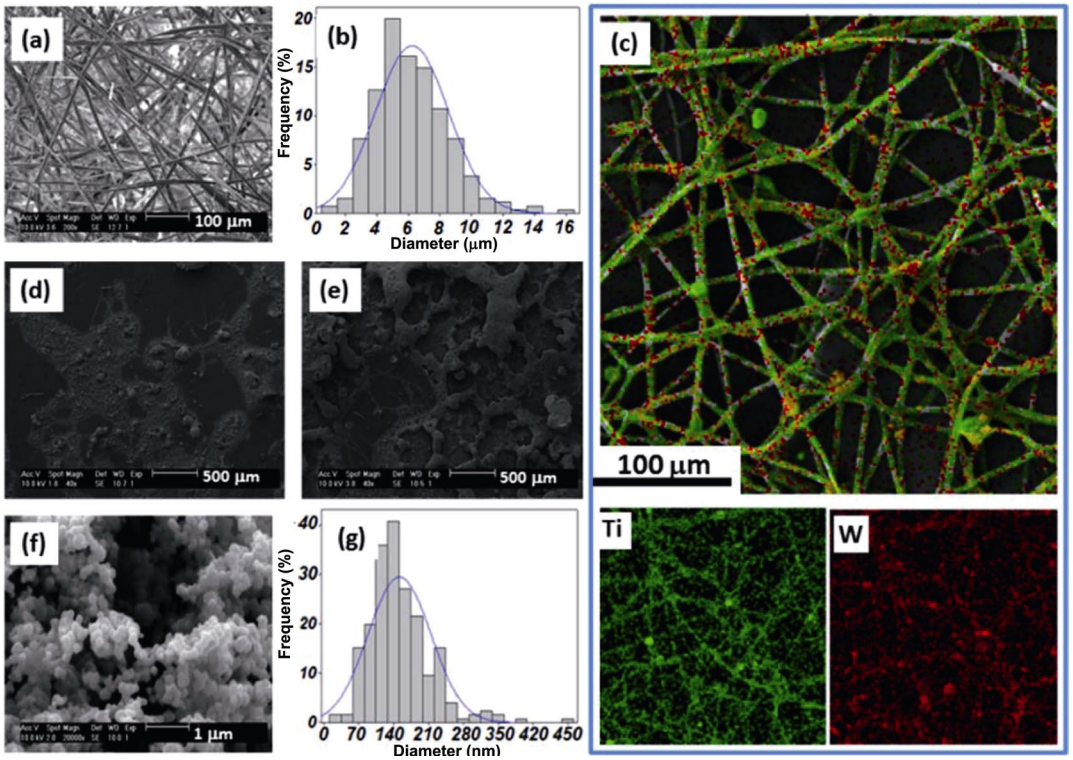


**Fig. 2** (a) SEM image of the ($TiO_2$/$WO_3$)-loaded fibers and (b) their respective diameter distribution and (c) EDS mapping, before sintering; top view micrographs of the systems prepared with (d) one and (e) three layers, after sintering; (f) SEM image of the sintered $TiO_2$/$WO_3$ structures and (g) their diameter distribution of grains.

Figure 2(a) shows the photomicrograph of the ($TiO_2$/$WO_3$)-loaded fibers, before sintering (intermediate material of the structure preparation). The fiber composite exhibits regularity of diameter, without apparent structural defects. In addition, the fiber size follows a normal distribution with a mean diameter of $6.4 \pm 1\mu m$, as shown in the frequency histogram in Fig. 2(b). This is a first indication that the electrospinning process is able to promote the distribution of the oxides along the microfibers. The respective EDS mapping (Fig. 2(c)) shows that Ti and W populations are evenly dispersed throughout the fibrous structure. The combination of these results demonstrates that the fibers act as a template to promote an adequate distribution of the oxides, to prevent further aggregation of the particles and increase the surface area of action of heterogeneous oxides (free of polymer) after the sintering process. This feature is quite important for the process of detecting moisture since it favors the adsorption of oxygen molecules.

After sintering, the polymer fibrous template is eliminated and it is possible to observe visual differences in the morphology of the resulting material (Figs. 2(d) and 2(e)) produced from 1 to 3 layers of fiber composite. As expected, the sintered material from 3 layers presents a higher amount of semiconductors than those produced with one layer of fibers, as a result of the higher number of layers deposited initially on the electrode. No significant microstructural difference is found in these two preparation configurations. The sintered $TiO_2$/$WO_3$ system presents spherical particles and a porous structure (Fig. 2(f)). The particle diameters also obey a normal distribution with an estimated average of $145.7 \pm 47$ nm (Fig. 2(g)).

The X-ray diffractograms of the non-sintered $TiO_2$/$WO_3$ oxides (encapsulated in the fibers) and sintered at 500 ℃ were analyzed (Fig. 3). The non-sintered samples (Fig. 3(a)) show the peaks determined at $2\theta$ = 25.2°, 36.9°, 37.8°, 38.5°, 48.1°, 53.9°, 55.0°, 62.8°, and 68.6°, attributed to the anatase $TiO_2$ with tetragonal crystalline structure and space group 141/*amd* [9,10]. The crystallographic parameters are $a = b = 3.7822$, $c = 9.5023$, and $\alpha = \beta = \gamma = 90°$. Data are in accordance with ICDD card 21-1272.

The monoclinic $WO_3$ signature, with space group $P21/n$ (parameters $a = 7.306$, $b = 7.540$, $c = 7.692$, $\alpha = \gamma = 90°$ and $\beta = 90.88°$) is observed at $2\theta$ = 23.1°, 23.6°, 24.2°, 28.6°, 34.0°, 35.5°, 41.8°, 44.0°,

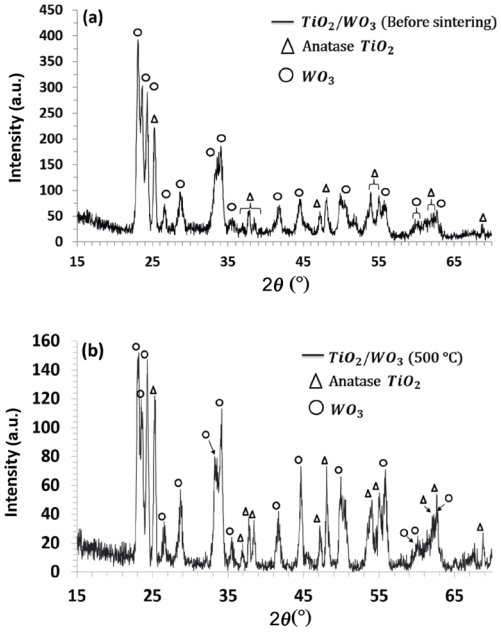


**Fig. 3** XRD spectra of (a) non-sintered $TiO_2/WO_3$ and (b) sintered nanostructures at 500 ℃.

55.7°, 59.8°, and 62.8°, and confirmed from the ICDD card 71-0131. No impurity is detected in the composite spectrum.

The spectrum of the sintered structures at 500 ℃ for 1 h shows the anatase $TiO_2$ and $WO_3$ peaks (previously verified in the non-sintered sample), indicating that the sintering process did not cause phase changes in the material (Fig. 3(b)). No additional peak is detected, but the peak intensity decreased according to the increase in the sintering temperature due to the increase in the degree of disorder in the resulting composite structure caused by the interaction between the oxides after sintering.

The Raman spectra of pristine $TiO_2$ and $TiO_2/WO_3$ structures sintered at 500 ℃ are shown in Fig. 4. The $TiO_2$ spectrum exhibits the characteristic vibrational modes of the anatase phase preserved after the sintering at 500 ℃, indicating that there is no change in the atomic arrangement of the semiconductor under these conditions (anatase is known to favor moisture adsorption). The signature of the six active vibration modes of $TiO_2$ ($3E_g + 2A_{1g} + B_{1g}$) is detected at 143 and 196 $cm^{-1}$ (both related to $E_g$ mode), 396 $cm^{-1}$ ($A_{1g}$), 516 $cm^{-1}$ ($A_{1g}$ / $B_{1g}$), and 637 $cm^{-1}$ ($E_g$) wavenumbers [15–19].

The $TiO_2$ characteristic bands are also detected in the $TiO_2/WO_3$ sintered system, but they are slightly shifted for smaller wavenumber values (red shifted) by approximately 10 $cm^{-1}$.

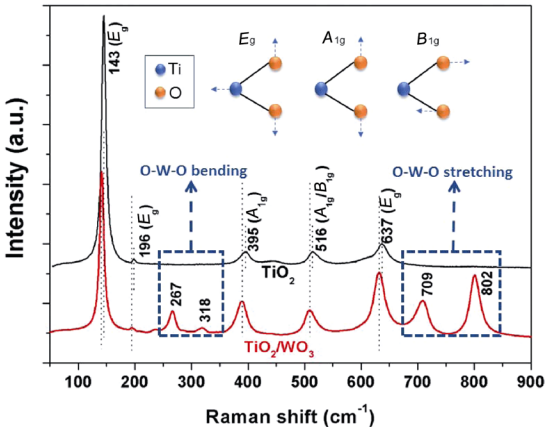


**Fig. 4** Raman spectra of pure $TiO_2$ and $TiO_2/WO_3$ nanostructures sintered at 500 ℃. In the inset, $E_g$, $A_{1g}$, and $B_{1g}$ vibrational motions of Ti and O atoms of $TiO_2$ are illustrated. The dotted lines help visualize the redshift of $TiO_2$ bands in sintered $TiO_2/WO_3$ nanostructures.

The tungsten has a covalent radius of 1.30 Å and ray to states $W^{6+}$ of the order of 0.62 Å. The titanium in the state $Ti^{4+}$ has an ionic radius of the order of 0.68 Å. With sintering, the $W^{6+}$ ions can be easily inserted inside the $TiO_2$ structure, according to number of the available vacancies, causing a small distortion in the $TiO_2$ structure. In the Raman spectra, this interaction promotes the shifting of characetristic vibrational bands of $TiO_2$ to smaller wave numbers (redshift). A redshift in Raman spectra is associated to relaxation in the surface and confinement of phonons [20], which favors the conduction processes in the material for applications such as humidity sensors.

The additional pairs of bands at 267 and 318 $cm^{-1}$, and at 709 and 802 $cm^{-1}$ are signatures of the O–W–O bending and stretching vibration modes of $WO_3$, respectively [21].

The combined analysis of the XRD and Raman results indicates that the $TiO_2$ / $WO_3$ heterogeneous material is polycrystalline, with no formation of new phases or solid solutions between the components.

### 3.2 Humidity sensing mechanism and electrical signature

The depicted and discussed data reflect the measurement done with three different acquisition runs using the same test temperature and moisture concentration. The plotted data are the mean value of all performed sets of measurements.

Two types of adsorption occur in the analyzed materials. For low levels of RH, chemisorption takes

place. As RH concentration is raised, physisorption replaces chemisorption. The chemisorbed coating is strongly tied to the semiconductor material. Once completed (in between 20%–40% RH), it will not be affected by RH increase. As RH increases, a physisorbed coating is formed over the previously chemisorbed layer. An increasing number of physisorbed coats will form on top of the previous one, as RH keeps increasing [22,23]. Differently from the chemisorbed layer, the physisorbed layers will be easily removed if the RH values decrease.

RH starts to condensate inside the pores of structures as two or more physisorbed water layers are formed. Electric polarization is mainly due to the charge movement when an external alternating electric field is used to excite the semiconductor. In this context, the capacitance of the material decreases as a result of the tight deposition of the moisture molecules arranged on top of each other [24]. The charge transporters accumulated at the grain–grain barrier also contribute to polarization [25,26].

Parallel to the chemisorption and physisorption phenomena, it is possible to observe that in the systems obtained in this work, the total conductance of the semiconductor composite passes through a minimum value. This behaviour is typical of a p- to n-type conduction transition [27–30]. When a p- to n-type transition occurs for small water coverage, it must be considered of electronic nature and the cause for the observed conduction transition can be explained by the band-like theory.

For low RH, a p-type conductivity is observed: the free electron concentration decreases once the charge carrier density also decreases. In other words, when exposed to a low density of humidified air at room temperature [27], oxygen is adsorbed in one or more of the species $O^-$, $O^{2-}$, $O_2^-$, and $O_2^{2-}$. During this phase, the impedance of the system increases, once electrons are being removed from the conduction band. Simultaneously, these oxygen species become available to react with moisture and the associated electrons are returned to the conduction band.

The velocity at which these two just above-mentioned reactions take place controls the overall resistance of the material with moisture. In the case of the $TiO_2$ / $WO_3$ films prepared by electrospinning, the surface area is much higher than the observed for pelletized systems. This configuration promotes a higher rate of oxygen adsorption that generates a large number of holes in the conduction band, than the rate at which water molecules are adsorbed, due to the low humidity concentration available near the surface. Consequently, at this stage the impedance of the materials increases.

Only for higher moisture concentrations (near the 40% RH and above), the rate at which both reactions occur is inverted and so the number of electrons present in the conduction band increases, with consequent decrease of the material impedance.

When RH is increased and physisorbed layers form, the impedance of the structures decreases as a consequence of proton hopping, of electronic and ionic diffusion, and of transport and polarization mechanisms.

As successive physisorbed water layers are formed, the progressive ionization of water (presence of $H_3O^+$ groups) produces a large number of charge carriers, according to Grotthuss mechanism [31]. The charge transport occurs when $H_3O^+$ releases a proton ($H^+$) to a nearby $H_2O$ molecule ($H_3O^+ \rightarrow H_2O + H^+$), ionizing it and forming another $H_3O^+$, resulting in the hopping of protons from one water molecule to another. This reaction induces a large amount of free electrons in the conduction band, originating a substantial reduction of the impedance, typical of n-type behaviour.

Electrical impedance spectroscopy helps highlighting the phenomena that contribute to overall electrical conduction of the material [24].

In all Nyquist diagrams (plot of imaginary part (Im$Z$) versus real part (Re$Z$) of impedance ($Z$)) of the $TiO_2$ / $WO_3$ systems as function of the RH (Figs. 5(a) and 5(b)), it is possible to notice a depression in the characteristic semicircles.

This means that two relaxation contributions are present, one arising from the conduction along the grain surface and a second from the conduction through grain boundaries [29]. Diffusion mechanisms are also present, but not clearly identifiable for all systems, since the characteristic straight line is not always visible: still, diffusion along the surface water layer (and in the interface with the electrodes) contributes to the electrical behavior of the structures (more evident for the higher RH concentrations).

For all preparation settings (1 or 3 layers and sintering at 500 ℃), the semicircles begin to increase in the range of low relative humidity values; from 40% RH, they change their behavior and begin to decrease progressively. This alteration is typical of a transition from p- to n-type conduction, as discussed previously.

As an example of that was analyzed, only graphs of the systems at 20 ℃ are presented (Figs. 5(a) and 5(b)). The complete description of this phenomenon for tested configurations can be verified in Fig. 6.

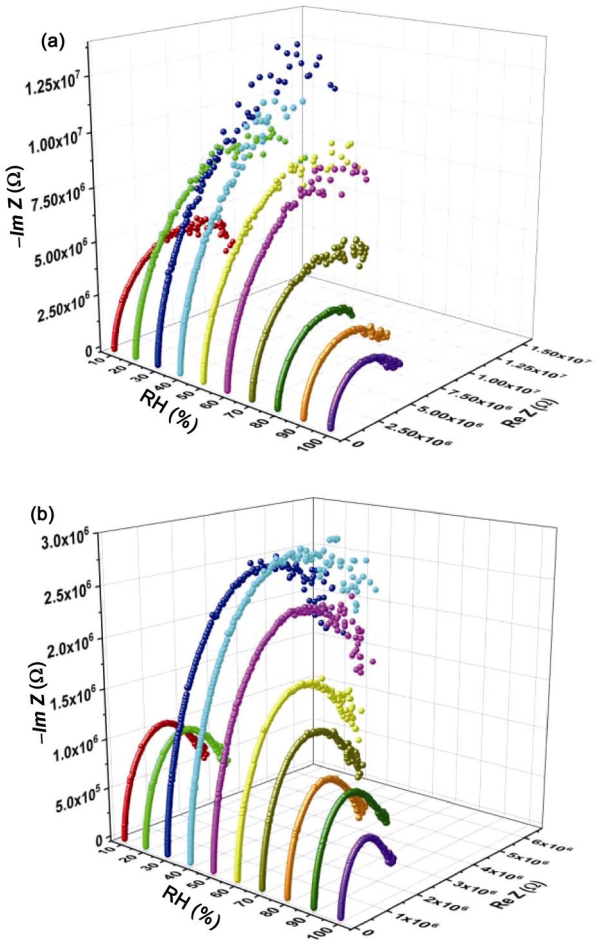


**Fig. 5** Nyquist diagrams of the $TiO_2/WO_3$ systems as function of RH, at 20 ℃: (a) 500 ℃, 1 layer; (b) 500 ℃, 3 layers.

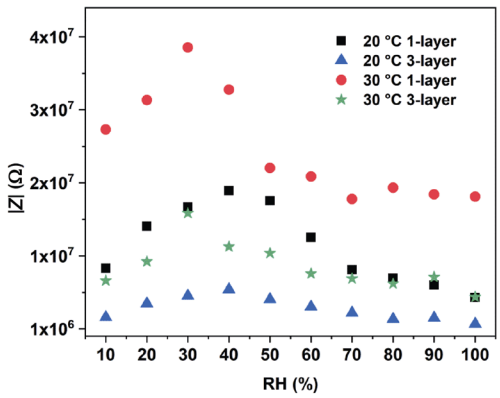


**Fig. 6** Impedance variation with RH (at 400 Hz) for the $TiO_2/WO_3$ structures at working temperatures of 20 and 30 ℃.

Figure 6 shows the impedance modulus (|*Z*|) of the $TiO_2/WO_3$ for all the preparation conditions, at working temperatures of 20 and 30 ℃, and for excitation frequency of 400 Hz. At both working temperatures, the structures show sensitivity to variations in relative humidity of the environment.

The systems prepared with three layers present advantage over the systems prepared with one layer, especially those sintered at 500 and 20 ℃ working temperature (|*Z*| relative variation of approximately one order of magnitude in the 40%–100% RH range).

For the studied systems in this work, the surface area appears to be higher than the pelletized systems [9,10], using a much smaller amount of material (2.24±0.21 mg by layer versus 2.0 g used to fabricate the volumetric pellets). The response of the new systems to humidity variation is different from the previous reported ones (n-type conduction) and has been improved: besides they are in harmony with the alterations of their structure (discussed in Section 3.1), consequence of the modification of the preparation process. The results also indicate that the prepared structures can be explored for the development of humidity-sensing devices that operate in specific ranges of RH, in particular from 40% to 100% RH [32–34].

Table 1 shows the long-term stability analysis for the $TiO_2/WO_3$ composite within 5 days, considering all combinations between the low (-) and high (+) levels of each parameter (*T* and *L*), in the potential range (40%–100% RH) for use of the system as a humidity detector. It is possible to observe that the composite returns low values of relative impedance variation (between the initial value ($Z_0$) and the value obtained after five exposing days ($Z_5$), $(Z_0 - Z_5)/Z_0$, at the tested RH (50%, 70%, and 90%), which indicates the good performance of the system at both operation temperatures (20 and 30 ℃). The relative importance of the number of layers and working temperature on the $TiO_2/WO_3$ system sensitivity was discussed in more detail.

**Table 1 Long-term stability of all tested combinations between number of fiber layers (*L*) and working temperature (*T*) parameters, at 50%, 70%, and 90% of relative humidity. The stability values were given with respect to the relative impedance variations of the systems in the interval of 5 days of measurement, under constant RH**

| | *T*(–) | | | *T*(+) | | |
|---|---|---|---|---|---|---|
| RH (%) | 50 | 70 | 90 | 50 | 70 | 90 |
| *L*(–) | 2.7% | 3.1% | 2.3% | 3.2% | 2.5% | 2.5% |
| *L*(+) | 2.2% | 2.8% | 1.8% | 2.1% | 2.7% | 2.8% |

### 3. 3 Relative importance of parameters

Table 2 shows the results obtained from impedance variation in the 40%–100% RH range for all combinations of the parameters studied in the process at 400 Hz. The variation in the impedance excursion is an indirect measure of the material sensitivity to the variations of humidity [35]. The importance of the parameters is not affected at excitation frequencies of superior magnitude (in the 400 Hz–40 MHz range).

The study realized by $2^2$ factorial design confirms the importance of parameters in the electrical response of the systems, in agreement with that was discussed in the previous section. Chemometrics shows that the combined action of the parameters can improve the sensitivity of the system under these conditions.

The increase in number of layers (*L* factor) positively favors to the response of the system (relative importance of +8.5). Based on the results in Table 2, it is possible to infer that the number of layers favors water adsorption at working temperature of 30 ℃, since the 3-layer samples increase the impedance variation of the system (|*Z*| variation of 51.65% to 68.17%). Using the same analysis, the relative variation of |*Z*| is slightly increased at 20 ℃ (73.46% to 73.90%).

From these analyses, it can be verified that the tested systems at 30 ℃ (Table 2) have the lowest values of impedance variation (negative influence of the *T* factor of 13.7). The increase in temperature promotes a thermal agitation in the system that hinders the formation of the physisorbed layers and, consequently, the electrical conduction processes in the material are less favored.

In summary, the 3-layer configuration improves the moisture sensitivity of $TiO_2$ / $WO_3$ structures at higher working temperatures. On the other hand, this factor does not offer a significant difference in the system sensitivity when used at 20 ℃. All comments discussed here justify the continuity of the studies using this fabrication route.

**Table 2 Impedance modulus variation of the $TiO_2$/$WO_3$ structures as response to the combination of studied *L* and *T* parameters. The symbols (-) and (+) represent the lowest and highest values of the parameters, respectively**

| Sample | Layer | Working temperature | *Z* variation (%) |
|---|---|---|---|
| *I* | – | – | 73.46 |
| *L* | + | – | 73.90 |
| *T* | – | + | 51.65 |
| *LT* | + | + | 68.17 |

## 4 Conclusions

The shape and size of the grains as well as the superior surface area/volume ratio of the composite obtained by the alternative procedure were decisive factors for the observation of a p- to n-type conduction transition and for good moisture sensitivity in the interval in between 40% and 100% RH. In addition, the alteration of the fabrication route promoted the redshift of the $TiO_2$ characteristic bands in Raman spectrum of the $TiO_2$ / $WO_3$ systems and an improvement in their RH-dependent electrical signature suggesting an effective titanium–tungsten interaction. The increase in the adsorption is directly related to combination of the analyzed parameters such as sintering temperature, number of fiber layers on the electrode, and working temperature.

### Acknowledgements

The corresponding author would like to thank Drs. Helinando Oliveira, Pedro Faia, Juliano Libardi, and Pedro Dicesar for the technical support. The authors also acknowledge the financial support from National Council for Scientific and Technological Development (CNPq - Brazil, Project 202451/2015-1) and Bahia State Research Foundation (FAPESB, Project 1252/2018).

### References

[1] Farahani H, Wagiran R, Hamidon MN. Humidity sensors principle, mechanism, and fabrication technologies: A comprehensive review. *Sensors* 2014, **14**: 7881–7939.

[2] Araújo ES, da Costa BP, Oliveira RAP, *et al.* $TiO_2$/ZnO hierarchical heteronanostructures: Synthesis, characterization and application as photocatalysts. *J Environ Chem Eng* 2016, **4**: 2820–2829.

[3] Faia PM, Ferreira AJ, Furtado CS. Investigations on humidity sensing properties of thick films of the $TiO_2$:$WO_3$ system. *Materials Science Forum* 2010, **636–637**: 307–314.

[4] Zhang D, Chang H, Li P, *et al.* Fabrication and characterization of an ultrasensitive humidity sensor based on metal oxide/graphene hybrid nanocomposite. *Sensor Actuat B: Chem* 2016, **225**: 233–240.

[5] Zhang D, Liu J, Xia B. Layer-by-layer self-assembly of zinc oxide/graphene oxide hybrid toward ultrasensitive humidity sensing. *IEEE Electron Device Lett* 2016, **37**: 916–919.

[6] Zhang D, Sun Y, Li P, *et al.* Facile fabrication of $MoS_2$-modified $SnO_2$ hybrid nanocomposite for ultrasensitive

humidity sensing. *ACS Appl Mater Interfaces* 2016, **8**: 14142–14149.

[7] Zhang D, Tong J, Xia B. Humidity-sensing properties of chemically reduced graphene oxide/polymer nanocomposite film sensor based on layer-by-layer nano self-assembly. *Sensor Actuat B: Chem* 2014, **197**: 66–72.

[8] Zhang D, Tong J, Xia B, *et al.* Ultrahigh performance humidity sensor based on layer-by-layer self-assembly of graphene oxide/polyelectrolyte nanocomposite film. *Sensor Actuat B: Chem* 2014, **203**: 263–270.

[9] Faia PM, Jesus EL, Louro CS. $TiO_2$:$WO_3$ composite humidity sensors doped with ZnO and CuO investigated by impedance spectroscopy. *Sensor Actuat B: Chem* 2014, **203**: 340–348.

[10] Faia PM, Libardi J, Louro CS. Effect of $V_2O_5$ doping on p- to n-conduction type transition of $TiO_2$:$WO_3$ composite humidity sensors. *Sensor Actuat B: Chem* 2016, **222**: 952–964.

[11] Nascimento MLF, Araujo ES, Cordeiro ER, *et al.* A literature investigation about electrospinning and nanofibers: Historical trends, current status and future challenges. *Recent Pat Nanotech* 2015, **9**: 76–85.

[12] Araújo ES, Libardi J, Faia PM, *et al.* Humidity-sensing properties of hierarchical $TiO_2$:ZnO composite grown on electrospun fibers. *J Mater Sci: Mater El* 2017, **28**: 16575–16583.

[13] Da Costa FFP, Araújo ES, Nascimento MLF, *et al.* Electrospun fibers of enteric polymer for controlled drug delivery. *Int J Polym Sci* 2015, **2015**: 1–8.

[14] Weissman SA, Anderson NG. Design of experiments (DoE) and process optimization. A review of recent publications. *Org Process Res Dev* 2015, **19**: 1605–1633.

[15] Fonoberov VA, Balandin AA. Interface and confined optical phonons in wurtzite nanocrystals. *Phys Rev B* 2004, **70**: 233205.

[16] Hearne GR, Zhao J, Dawe AM, *et al.* Effect of grain size on structural transitions in anatase$TiO_2$: A Raman spectroscopy study at high pressure. *Phys Rev B* 2004, **70**: 134102.

[17] Sahoo S, Arora AK, Sridharan V. Raman line shapes of optical phonons of different symmetries in anatase $TiO_2$ nanocrystals. *J Phys Chem C* 2009, **113**: 16927–16933.

[18] Horprathum M, Eiamchai P, Chindaudom P, *et al*. Oxygen partial pressure dependence of the properties of $TiO_2$ thin films deposited by DC reactive magnetron sputtering. *Procedia Eng* 2012, **32**: 676–682.

[19] Landmann M, Rauls E, Schmidt WG. The electronic structure and optical response of rutile, anatase and brookite $TiO_2$. *J Phys: Condens Matter* 2012, **24**: 195503.

[20] Yang CC, Li S. Size-dependent Raman red shifts of semiconductor nanocrystals. *J Phys Chem B* 2008, **112**: 14193–14197.

[21] Su CY, Lin HC, Lin CK. Fabrication and optical properties of Ti-doped $W_{18}O_{49}$ nanorods using a modified plasma-arc gas-condensation technique. *J Vac Sci Technol B* 2009, **27**: 2170–2174.

[22] Fripiat JJ, Jelli A, Poncelet G, *et al*. Thermodynamic properties of adsorbed water molecules and electrical conduction in montmorillonites and silicas. *J Phys Chem* 1965, **69**: 2185–2197.

[23] Anderson JH, Parks GA. Electrical conductivity of silica gel in the presence of adsorbed water. *J Phys Chem* 1968, **72**: 3662–3668.

[24] Macdonald JR. *Impedance Spectroscopy*. New york: John Wiley & Sons, 1987.

[25] Geng W, Yuan Q, Jiang X, *et al.* Humidity sensing mechanism of mesoporous MgO/KCl–$SiO_2$ composites analyzed by complex impedance spectra and bode diagrams. *Sensor Actuat B: Chem* 2012, **174**: 513–520.

[26] Bauerle JE. Study of solid electrolyte polarization by a complex admittance method. *J Phys Chem Solids* 1969, **30**: 2657–2670.

[27] Mönch W. *Semiconductor Surfaces and Interfaces*. Berlin, Heidelberg: Springer Science & Business Media, 2001.

[28] Gurlo A, Sahm M, Oprea A, *et al.* A p- to n-transition on α-$Fe_2O_3$-based thick film sensors studied by conductance and work function change measurements. *Sensor Actuat B: Chem* 2004, **102**: 291–298.

[29] Bârsan N, Grigorovici R, Ionescu R, *et al.* Mechanism of gas detection in polycrystalline thick film $SnO_2$ sensors. *Thin Solid Films* 1989, **171**: 53–63.

[30] Bayhan M, Kavasoğlu N. A study on the humidity sensing properties of $ZnCr_2O_4$–$K_2CrO_4$ ionic conductive ceramic sensor. *Sensor Actuat B: Chem* 2006, **117**: 261–265.

[31] Agmon N. The Grotthuss mechanism. *Chem Phys Lett* 1995, **244**: 456–462.

[32] Information on http://www.kesarcontrol.com/humidity.html.

[33] TDK Humidity Sensor CHS Series. Information on http://pdf.directindustry.com/pdf/tdk-electronics-europe/humidity-sensor-chs-series/34778-654990.html.

[34] Vent-Axia Ecotronic Humidity Sensor. Information on https://www.vent-axia.com/product/ecotronic-humidity-sensor.

[35] Suri K, Annapoorni S, Sarkar A, *et al.* Gas and humidity sensors based on iron oxide–polypyrrole nanocomposites. *Sensor Actuat B: Chem* 2002, **81**: 277–282.

**Open Access** This article is licensed under a Creative Commons Attribution 4.0 International License, which permits use, sharing, adaptation, distribution and reproduction in any medium or format, as long as you give appropriate credit to the original author(s) and the source, provide a link to the Creative Commons licence, and indicate if changes were made.

The images or other third party material in this article are included in the article's Creative Commons licence, unless indicated otherwise in a credit line to the material. If material is not included in the article's Creative Commons licence and your intended use is not permitted by statutory regulation or exceeds the permitted use, you will need to obtain permission directly from the copyright holder.

To view a copy of this licence, visit http://creativecommons.org/licenses/by/4.0/.